JOURNAL OF GEOPHYSICAL RESEARCH, VOL. 100, NO. A2, PAGES 1611-1624, FEBRUARY 1, 1995

One-dimensional hybrid satellite track model for the Dynamics Explorer 2 (DE 2) satellite

Wei Deng,[1,5] T. L. Killeen,[1] A. G. Burns,[1] R. M. Johnson,[1] B. A. Emery,[2]
R. G. Roble,[2] J. D. Winningham,[3] and J. B. Gary[4]

Abstract. A one-dimensional hybrid satellite track model has been developed to calculate the high-latitude thermospheric/ionospheric structure below the satellite altitude using Dynamics Explorer 2 (DE 2) satellite measurements and theory. This model is based on Emery et al. (1985) satellite track code but also includes elements of Roble et al. (1987b) global mean thermosphere/ionosphere model. A number of parameterizations and data handling techniques are used to input satellite data from several DE 2 instruments into this model. Profiles of neutral atmospheric densities are determined from the MSIS-90 model and measured neutral temperatures. Measured electron precipitation spectra are used in an auroral model to calculate particle impact ionization rates below the satellite. These rates are combined with a solar ionization rate profile and used to solve the O^+ diffusion equation, with the measured electron density as an upper boundary condition. The calculated O^+ density distribution, as well as the ionization profiles, are then used in a photochemical equilibrium model to calculate the electron and molecular ion densities. The electron temperature is also calculated by solving the electron energy equation with an upper boundary condition determined by the DE 2 measurement. The model enables calculations of altitude profiles of conductivity and Joule heating rate along and below the satellite track. In a first application of the new model, a study is made of thermospheric and ionospheric structure below the DE 2 satellite for a single orbit which occurred on October 25, 1981. The field-aligned Poynting flux, which is independently obtained for this orbit, is compared with the model predictions of the height-integrated energy conversion rate. Good quantitative agreement between these two estimates has been reached. In addition, measurements taken at the incoherent scatter radar site at Chatanika (65.1° N, 147.4° W) during a DE 2 overflight are compared with the model calculations. A good agreement was found in lower thermospheric conductivities and Joule heating rate.

1. Introduction

Comprehensively instrumented satellites have been used to study high-latitude thermosphere and ionosphere processes for a number of years. The Dynamics Explorer 2 (DE 2) satellite, in particular, was instrumented to measure auroral particles and fields, as well as neutral atmospheric and ionospheric parameters within the high-latitude thermosphere. These measurements have greatly improved our understanding of the various physical processes in this region. However, a significant gap in knowledge and understanding still exists in the lower thermosphere/ionosphere due to relative inaccessibility of this region to direct experimental approaches. Several detailed numerical models have been developed to study the dynamics and energetics of the thermosphere and ionosphere, including the lower thermospheric region. In particular, the National Center for Atmospheric Research thermosphere-ionosphere general circulation model (NCAR-TIGCM) has had a large measure of success in calculating wind and temperature fields similar to those observed from the DE 2 satellite [*Hays et al.*, 1984; *Roble et al.*, 1984; *Killeen et al.*, 1986; *Killeen and Roble*, 1988]. A one-dimensional global mean thermosphere/ionosphere/mesosphere model has also been developed to study the global average structure in this region within the framework of NCAR-TIGCM [*Roble et al.*, 1987; *Roble and Dickinson*, 1989]. The calculated global average structure from this model compares well with the globally averaged structure determined from ionospheric and thermospheric empirical models.

Large scale numerical models such as the NCAR-TIGCM require the parameterization of auroral energy and momentum inputs to the neutral thermosphere. The AMIE technique of *Richmond and Kamide* [1988] uses a data assimilation method to provide such inputs and is critically dependent on knowledge of the ionospheric conductivities in the lower thermospheric dynamo region. The study of energy exchange

[1]Space Physics Research Laboratory, Department of Atmospheric, Oceanic and Space Sciences, University of Michigan, Ann Arbor.
[2]National Center for Atmospheric Research, Boulder, Colorado.
[3]Department of Space Sciences, Southwest Research Institute, San Antonio, Texas.
[4]University of Texas at Dallas, Richardson.
[5]Now at Haystack Observatory, Massachusetts Institute of Technology, Westford.

Paper number 94JA02075.
0148-0227/95/94JA-02075$05.00

between the magnetosphere and ionosphere also requires detailed information on Joule heating rates in the lower thermosphere. It is therefore of value to develop a "satellite track" model that uses direct satellite measurements in the upper thermosphere to estimate the conductivity and Joule heating rates in the lower thermosphere.

Several satellite-based empirical models have been constructed to describe electric conductivities [*Wallis and Budzinski*, 1981; *Fuller-Rowell and Evans*, 1987], electric fields [*Heppner*, 1977; *Heelis et al.*, 1982; *Foster*, 1983] and Joule heating [*Foster et al.*, 1983; *Heelis and Coley* 1988]. *Emery et al.* [1985] developed a satellite track model that uses the DE 2 measurements to calculate the ionospheric/thermospheric structure down to about 80 km below the satellite orbit. This model has also been used to study the Joule heating rate in the lower thermosphere and mesosphere for a proton auroral event [*Roble et al.*, 1987a], but these model predictions have not been compared with direct experimental data from the lower thermosphere. In this paper, we extend the work of Emery et al. to include the ionospheric processes that are modeled in the global mean thermosphere/ionosphere model. The extended model is then used to study the ionospheric structures below a single satellite orbit from October 25, 1981. We also compare the model predictions of the height-integrated energy conversion rate with the field-aligned Poynting flux, which is independently calculated for this orbit (J. B. Gary et al., Examples of Poynting vector determination using DE-B satellite data, submitted to *Journal of Geophysical Research*, 1994) (hereinafter referred to as Gary et al. submitted manuscript, 1994). Finally, We compare the extended satellite track model predictions with measurements taken at the incoherent scatter radar site at Chatanika (65.1° N, 147.4° W) during a DE 2 overflight.

2. Model

The earlier version of the satellite track model was described in detail by *Emery et al.* [1985]. Briefly, it uses DE 2 measurements of energetic electron spectra in an auroral code to determine the particle ionization rates. The measured ion drifts and electron densities at satellite altitude, as well as a model of solar flux, are also used as model inputs. The profile of electron and ion densities, temperatures, conductivities and Joule heating rates, as well as particle and solar heating rates, are calculated from these inputs in a neutral atmosphere modified to reproduce the measured temperature and O/N_2 ratio at the satellite altitude.

We have extended the Emery et al. satellite track code using a hybrid approach. In this scheme, we utilize the global mean thermosphere/ionosphere code of *Roble et al.* [1987b] to model the ionospheric processes below the satellite orbit theoretically. Empirical and semi-empirical models such as MSIS-90 [*Hedin et. al.*, 1991] and the VSH [*Killeen et al.*, 1987] model are used to determine the neutral atmosphere structure and winds.

The solar EUV and UV fluxes are obtained from the empirical solar flux model of *Hinteregger* [1981] that is based on the Atmosphere Explorer Satellite measurements. The solar EUV and UV flux model parameterizes the solar flux into 59 wavelength bands and emission lines. These wavelengths have been specified by *Torr et al.* [1979] and *Torr and Torr* [1985] along with the effective absorption and ionization cross sections. This parameterized version of the solar flux is used in the global mean model and is adopted in our model to calculate the photoionization rate with some modifications for calculating the solar zenith angle at each position along the satellite track. The ionization caused by secondary photoelectrons is also calculated in our model using the analytical expression of *Richards and Torr* [1988].

The auroral ionization rates are calculated following the method of *Rees* [1963, 1969]. The electron flux needed in this calculation is determined from the low-altitude plasma instrument (LAPI) measurements. The calculated auroral ionization rate at each altitude and latitude below a satellite track is added to the photoionization rate to determine the total ionization rate for the calculation of ion and electron densities.

The one-dimensional O^+ diffusion equation derived by *Roble et al.* [1987b] is solved in a vertical constant pressure surface coordinate system, using the calculated total ionization rates. This vertical coordinate system consists of 13 pressure levels ranging from approximately 97 to 600 km. The use of a pressure coordinate system insures that the normalized ionization rates determined from the DE 2 electron flux spectra are independent of atmospheric model parameters [*Fuller-Rowell and Evans*, 1987]. The upper boundary conditions of this equation are determined by the DE 2 electron density measurements, with an assumption that O^+ is the dominant ion at the satellite altitude. The lower boundary condition assumes photochemical equilibrium. The one-dimensional O^+ diffusion equation solved here does not include the horizontal transport. In the E and F_1 region the neglect of horizontal transport is justified because photochemical time constants are fast compared to the transport time constant. In the F_2 region, however, horizontal transport can have an important influence on the O^+ and hence on the electron density distributions. Because NO^+, O_2^+, and N_2^+ are much shorter lived, photochemical equilibrium is assumed throughout the thermosphere for these species. Their distribution is thus calculated using a photochemical equilibrium code developed by *Roble et al.* [1987b]. By combining the production and loss terms of these species, a fourth-order equation for electron density may be derived. The quadratic equation is solved using the procedures discussed by *Roble and Ridley* [1987].

The global mean thermosphere/ionosphere model also allows us to solve the electron and ion energy equations. The one-dimensional electron energy equation [*Schunk and Nagy*, 1978] is solved by considering photoelectron heating as the main source term and the electron-neutral elastic and inelastic collision processes as the main loss terms. The upper boundary condition of this equation is determined by the electron temperature measurement at the satellite orbit. The lower boundary condition of this equation is set equal to the neutral temperature calculated by the MSIS-90 model. The ion temperature is then calculated by considering the local thermal equilibrium between the ions and neutrals, including the Joule heating specified from the satellite measurements and VSH neutral winds.

The Pedersen and Hall conductivities are determined using

the calculated electron and ion densities and temperatures. In order to determine the Joule heating rate, we have used the satellite measured ion drift vector to derive the electric field in a background magnetic field which is measured at the satellite orbit. This electric field is then assumed to map downward along the magnetic field lines. The neutral wind vector profiles needed in the Joule heating calculation are obtained from the VSH model. The measured neutral winds are used as a guide to adjust the *Ap* value in the VSH model so that it could reasonably reproduce the measurements at the satellite altitude.

3. DE 2 Measurements From Orbit 1222

The Dynamics Explorer 2 satellite passed over the southern hemisphere polar cap on orbit 1222 between 0500 and 0545 UT on October 25, 1981. Simultaneous measurements from a number of instruments carried onboard the satellite are used as input to the satellite track model. The particle spectra are obtained using the LAPI [*Winningham et al.*, 1981]. The ion drifts are obtained by combining the zonal and meridional components from the ion drift meter (IDM) [*Heelis et al.*, 1981], and the retarding potential analyzer (RPA) [*Hanson et al.*, 1981] instruments, respectively. The neutral winds are measured by the Fabry-Perot interferometer (FPI) [*Hays et al.*, 1981] and the wind and temperature spectrometer (WATS) [*Spencer et al.*, 1981]. In addition to these instruments, the Langmuir probe (LANG) [*Krehbiel et al.*, 1981] and the neutral atmosphere composition spectrometer (NACS) [*Carignan et al.*, 1981] measure the electron density, temperature and neutral constituent abundance. The magnetic fields are measured by the DE 2 magnetometer (MAG-B) [*Farthing et al.*, 1981].

Figure 1 shows a summary of observed plasma and neutral gas parameters which are plotted as a function of universal time for a DE 2 pass (orbit 1222). As can be seen from the lower left panel, this orbit occurred during relatively active geomagnetic conditions. The *Kp* index was about 5 and the IMF *Bz* was southward during the DE 2 pass. The ion drifts for this orbit depict a conventional two-cell pattern with an antisunward velocity of about 500 m/s in the polar cap. The ion drifts are used to determine the electric field in a background magnetic field measured by MAG-B.

The measured neutral winds and ion drifts show close agreement in magnitude and direction throughout the dusk auroral

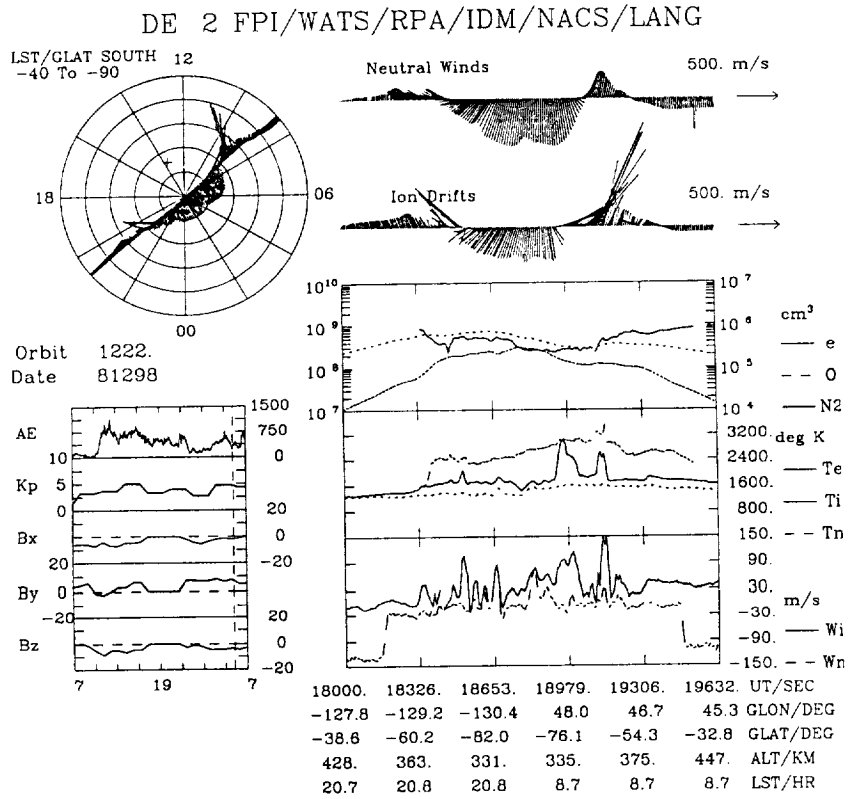

Figure 1. A summary of DE 2 measurements during orbit 1222. The neutral winds and ion drifts are shown in the top two traces plotted against time, attitude, and altitude of the spacecraft as it passes (left-to-right) over the southern hemisphere (summer) polar region. The second panel shows the atomic oxygen and nitrogen densities and electron density. The third panel shows the electron, ion and neutral temperatures. The bottom trace shows the measured vertical winds and ion drifts. The lower inset to the left shows the time history of the IMF components and the geophysical indices *AE* and *Kp* for 24 hours prior to the orbital pass. The mid-point UT for the satellite pass is denoted by the vertical dotted line. The upper inset to the left shows a polar dial (geographic latitude and solar local time) for the pass, with the neutral winds and ion drifts plotted and the location of the geomagnetic pole given by the cross.

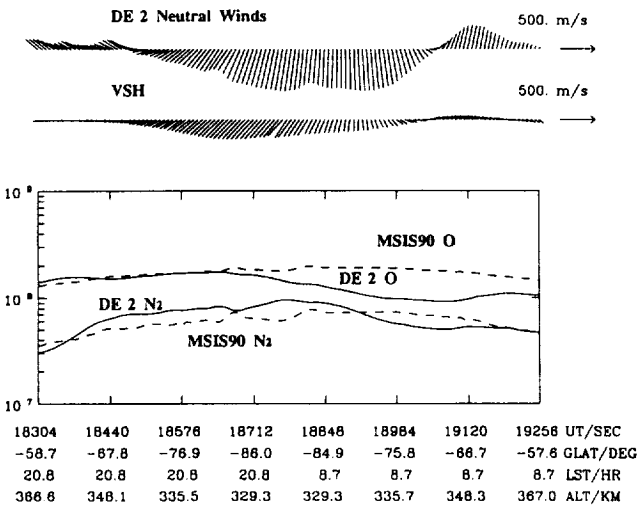

Figure 2. Comparison of DE 2 measurements during orbit 1222 with the VSH and MSIS-90 models. The neutral wind measurements are shown in the top trace. The second trace depicts VSH model calculations along the satellite track. Composition measurements for N2 and O (solid line) are plotted in the second panel. Also shown are MSIS-90 values calculated at the satellite altitude. The DE 2 measured neutral temperature is used to adjust the exospheric temperature in MSIS-90 model.

zone and polar cap but demonstrate larger differences in velocities in the dawn convection channel where the neutral winds move in the opposite direction in the higher latitude regions and respond only moderately to the strong sunward ion flow in the lower latitude region. In response to these large velocity differences, the ion temperature shows large increases (~1000 K) in the dawn convection channel. These increases are caused by enhanced frictional heating.

The VSH model of *Killeen et al.* [1987] was used to provide neutral wind profiles below the satellite orbit during an active geomagnetic period. Figure 2 shows a comparison of VSH predicted neutral winds with the satellite measurements. Although there are significant differences in detail, the VSH-calculated winds show sufficient similarity with the satellite measurements (antisunward polar cap flow, bounded by moderate and partially sunward flow in the auroral regions). The calculated wind altitude profiles are used in the satellite track model to determine the Joule heating rate.

The MSIS-90 model was used to provide the compositional structure below the satellite orbit. The number densities for N_2 and O calculated from the modified MSIS-90 model along the satellite track are plotted in the bottom panel of Figure 2 (dashed lines). The DE 2 measurements for these two constituents are also shown in Figure 2 (solid lines) for the same orbit. In this calculation, we have adjusted the exospheric temperature of the MSIS-90 model to the neutral temperature measured at the satellite altitude without any changes in the model inputs and lower boundary conditions. Comparison between model calculated temperature with that measured by the satellite suggests this is a reasonable adjustment for this orbit. This adjusted MSIS-90 model is then used in the satellite track model to derive the compositional structure below the satellite altitude.

A factor of 2 difference in [O] density between the model calculation and satellite measurement is observed in the morning auroral region. The effects of this difference on model calculated electron density and Joule heating are discussed in the next section. It is very difficult for MSIS-90 model to make an accurate prediction on composition changes in the auroral region, especially during a geomagnetic storm. We plan to improve our model by using a newly developed storm time VSH model which promises some improvements in composition changes at high latitude thermosphere.

The electron precipitation flux along the DE 2 track was measured by LAPI. Plate 1a shows the downward electron energy flux averaged over pitch angles from 0° to 90°. These fluxes are detected from the LAPI instrument in the energy range from the 5 eV to 31 keV. The increase of electron flux is seen both in the morning and the evening auroral regions. A large scale precipitation enhancement exists in the evening auroral zone, while in the morning auroral region there are only some discrete auroral arcs. The energetic electron precipitation in the polar cap is found to be very small. These measured electron flux spectra are used to determine the auroral ionization rate below the satellite orbit as described earlier.

4. Model Calculations

The calculated particle ionization rate is shown in Plate 1b as a function of altitude in the satellite orbit plane. This ionization rate is derived from the LAPI instrument. Two regions of intense ion production are found in the morning and evening auroral ovals. These enhancements in the ion production rate are mainly caused by the energetic particles that are observed in the auroral regions. Hard electrons have enough energy to penetrate into the lower thermosphere and produce enhanced ionization in the *E* region, with maximum rates of 3.0×10^4 cm^{-3} and 2.6×10^4 cm^{-3} near 115 km in the morning and evening auroral region respectively. The polar cap is characterized by a soft particle drizzle. These particles produce less intense ionization in this region. In addition to this particle ionization, the solar photoionization production rate must be taken into account, since a part of this orbit is in the sunlit polar cap. Plate 1d shows the total ionization rate which combines the ion production rate from these two sources. The morning auroral oval is sunlit, therefore solar photoionization dominates most of the ion production in the *F* region. Particle precipitation is only important within the *E* region where few solar photons penetrate. In the evening auroral zone, however, particle precipitation dominates the total ion production rate at all altitudes below the satellite orbit. Within the polar cap, the ionization rate is controlled by solar photoproduction again. The total ionization rate is used as an input to determine the electron and ion densities in the satellite track model.

Plate 1c illustrates the calculated electron density below the satellite orbit. Energetic particles in the auroral region enhance the electron density at lower altitudes (*E* region) with a peak electron density of $\sim4.4\times10^5$ cm^{-3} at 115 km near 72°S geographic latitude. The electron density in the evening auroral zone is highly irregular due to the dominance of particle pre-

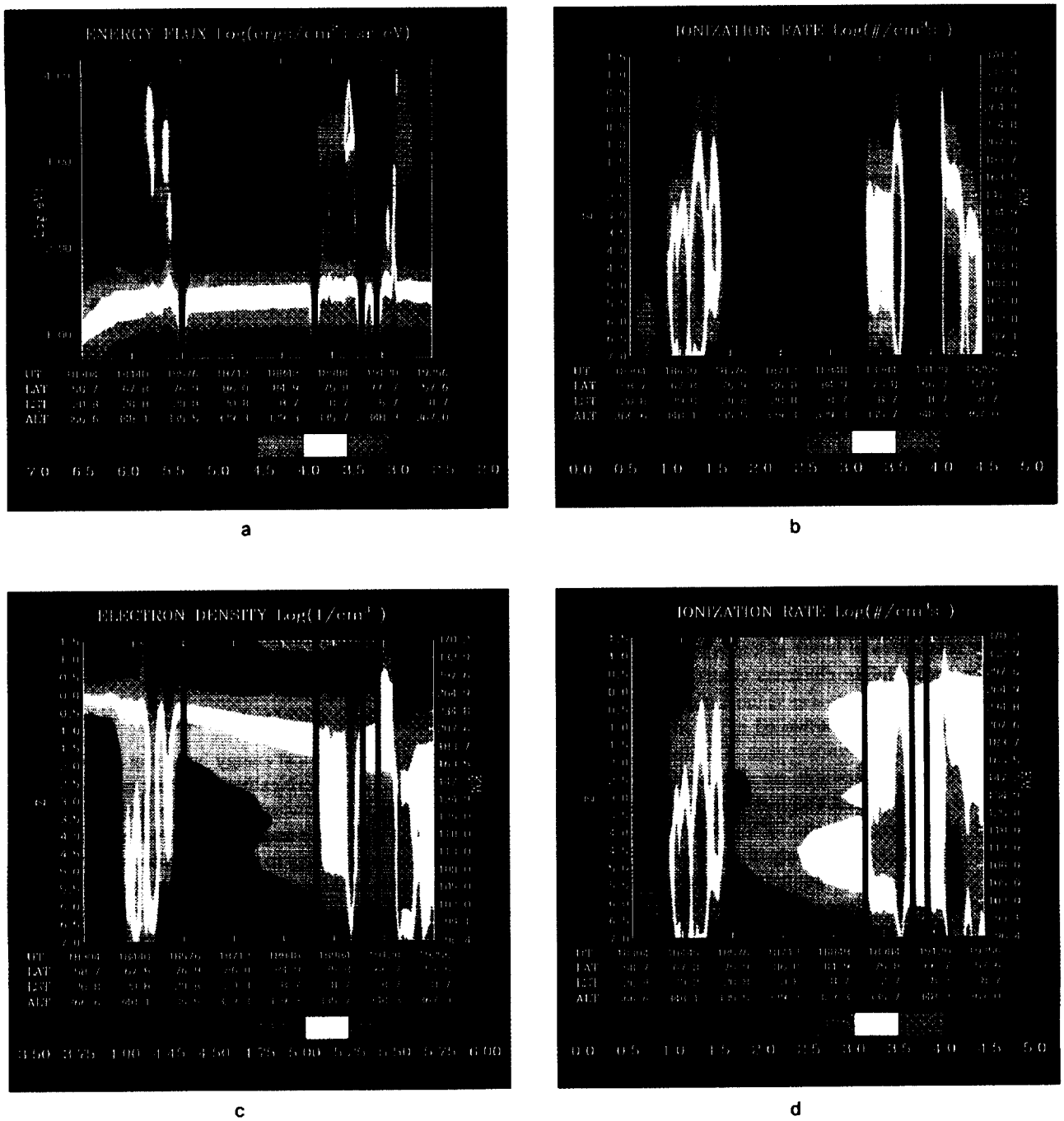

Plate 1. (a) Eight-second average of electron energy spectrograms for the downward electron precipitation measured along orbit 1222. The model calculated parameters below this orbit are plotted as a function of time along the orbital track of the satellite for (b) auroral ion production rate in log[cm^{-3} s^{-1}], (c) electron density in log[cm^{-3} s^{-1}], and (d) total ion production rate in log [cm^{-3} s^{-1}].

cipitation. It is clear that there exists a definite correlation between the enhancement of particle precipitation in the auroral region and the increase of the electron density in the lower thermosphere. In contrast to the particle-dominated auroral regions, the electron distribution in the polar cap is less irregular, increasing with decreasing solar zenith angle.

Electron and ion temperatures are depicted in Figures 3 and 4, respectively. The electron and ion temperatures vary smoothly in the satellite orbit plane except in the auroral regions. Outside the auroral regions, the ion temperature is lower than the electron temperature at higher altitudes, indicating that energy is transferred from the electrons to the ions through Coulomb collisions in these regions. However, inside the auroral oval, the ion temperature becomes highly structured and can even exceed the electron temperature. This occurs because the ion temperature responds directly to the Joule heating, thus leading to the increase in magnitude.

The electron and ion temperatures and densities discussed

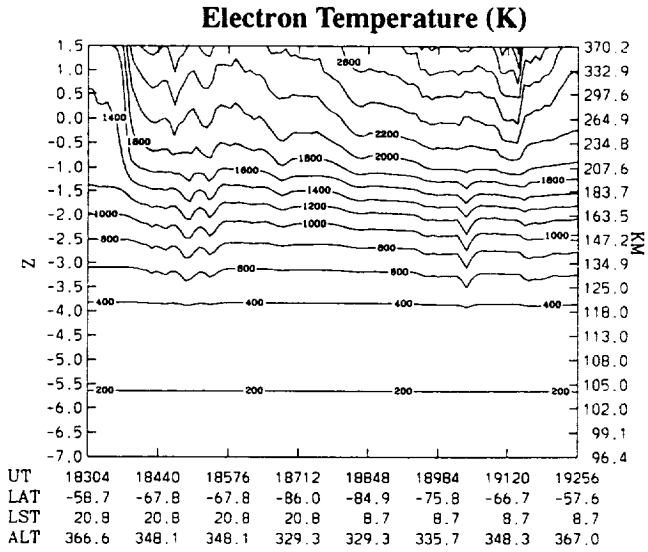

Figure 3. Contours of electron temperature calculated below satellite orbit 1222.

above are used to calculate the Hall and Pedersen conductivities. Plate 2a and 2b show this calculation. The Pedersen conductivity peaks in the region near 125 km, while the Hall conductivity maximizes at lower altitudes between ~100 and 120 km. The precipitating electrons contribute to the large enhancement of the conductivities in the *E* region auroral oval. This enhancement is less pronounced in the polar cap, which is dominated by solar photoionization. The height-integrated Hall and Pedersen conductivities are shown in Figure 5. Two peaks for Hall and Pedersen conductivities are found within the morning auroral region near 72°S and 64°S, with maximum values of the Hall conductivity of about 35 mhos. Within the evening auroral oval the height-integrated Hall and Pedersen conductivities have more irregular structures, with amplitudes between 5 and 18 mhos. The height-integrated Hall conductivity is larger than the height-integrated Pedersen conductivity in the auroral regions, reflecting the harder auroral particle precipitation which produces ionization in the lower *E* region rather than at higher altitude where Pedersen conductivity dominates.

The calculated Joule heating rates in the satellite orbit plane are shown in Plate 2d. The largest Joule heating rate occurs in the morning auroral region where large ion drifts are observed (Figure 1). The maximum rate is about 6×10^{-6} ergs/cm^{3}s at 125 km near 67°S. Another enhancement ir Joule heating is found in poleward of this auroral region, corresponding to the region of large velocity shear between the neutrals and the ions. The frictional heating resulting from the ion-neutral velocity difference enhances the Joule heating rate, which reaches a peak value of about 10^{-6} ergs/m^{3}s at 125 km. Another enhancement is located in the evening auroral region with a smaller magnitude. The Joule heating rate is smaller in the polar cap than in the auroral zone because the neutral wind moves in the same direction as the ion drift in this region, which reduces the frictional heating rate.

The factor of 2 difference in [O] density seen in Figure 2 may have a significant effect on the electron density and Joule heating rate. To estimate this effect, we have constructed a new [O] density profile by changing the exospheric temperature in the MSIS-90 model so that the calculated [O] density is reduced by one half at satellite altitude (340 km). We use this profile of [O] density to simulate what would happen in compensating the factor 2 difference seen in Figure 2 and run our model with the input specified at a point in the auroral region. A decrease in electron density by as much as 30% is observed at the F_2 peak. However, little change is found in the region below 220 km. Since the Joule heating rate peaks in the lower thermosphere and decreases rapidly with the increase of altitude, this change is less important to the height integrated Joule heating rate (in this case it is less than 5%).

The neutral gas heating rate due to particle precipitation is shown in Plate 2c. The particle heating rate is obtained by multiplying a neutral heating efficiency for auroral particle precipitation given by *Rees et al.* [1983, Figure 7] to the auroral ionization rate shown in Plate 1b. Neutral heating efficiency has a value of about 55% up to an altitude of 200-250 km and then decreases above this altitude. The particle heating rate is considerably smaller than the Joule heating rate in most regions below the satellite orbit, but is important in the auroral regions where it can even exceed the Joule heating rate below 100 km. The neutral gas heating rates discussed here will be used in the next section to study the electrical energy budget below the satellite orbit.

5. Poynting Flux and Joule Heating

The study of the electrical energy budget in the lower thermosphere/ionosphere is critically dependent on the electrical energy exchange rate between this region and the magnetosphere. In most cases, the magnetosphere/solar wind dynamo is a source of electric energy to the high-latitude thermosphere/ionosphere. Some of this energy is dissipated in the lower thermosphere by Joule heating. The rest is converted into neutral mechanical energy through Lorentz energy transfer. The

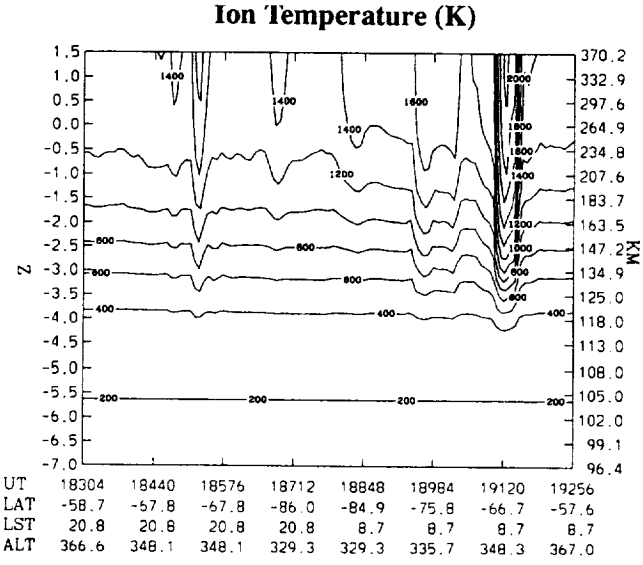

Figure 4. Contours of ion temperature calculated below satellite orbit 1222.

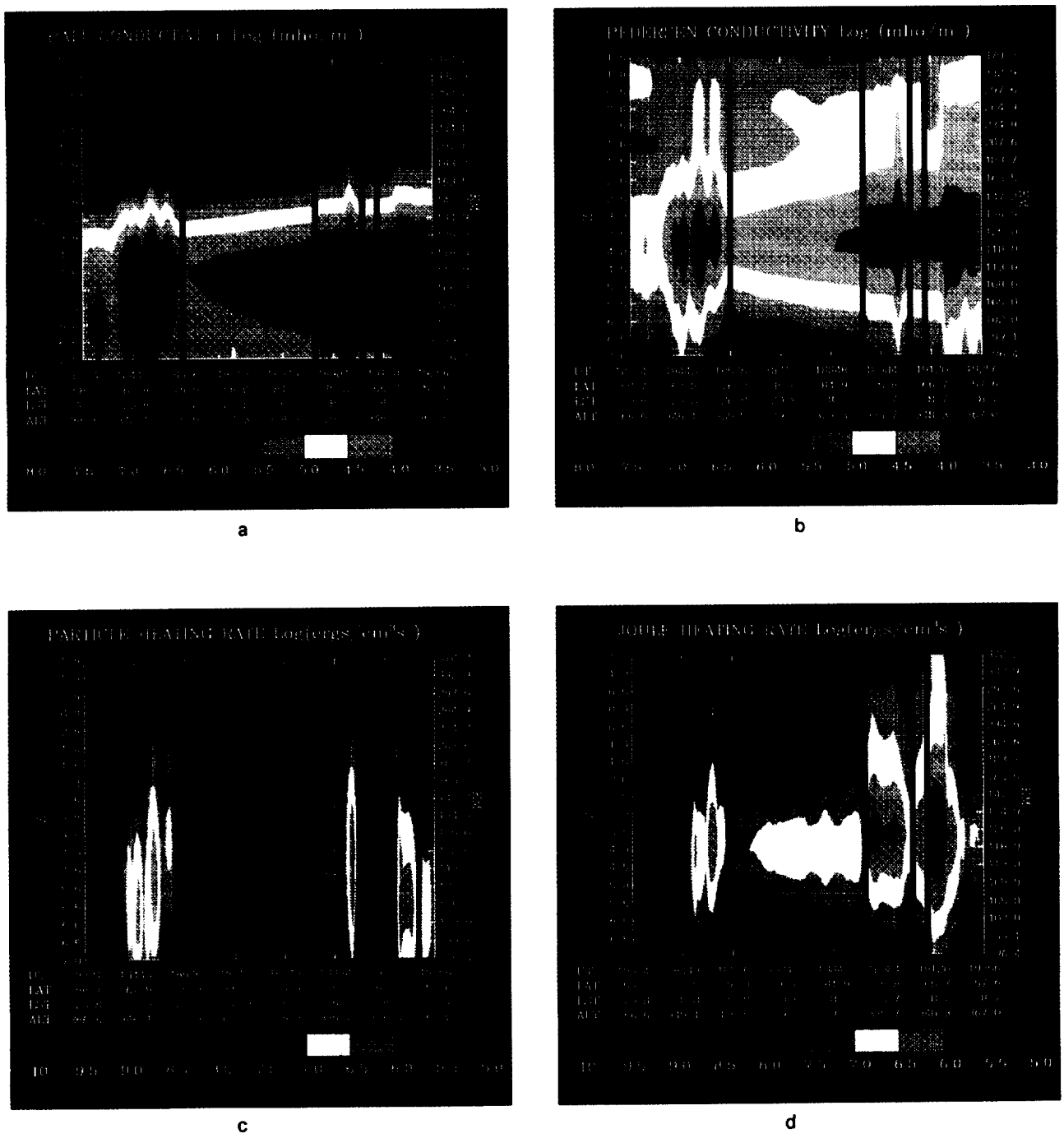

Plate 2. The model calculated parameters below satellite orbit 1222 for (a) Hall conductivity in log[mho/m], (b) Pedersen conductivity in log[mho/m], (c) particle heating rate in log[ergs cm^{-3} s^{-1}], and (d) Joule heating rate in log[ergs cm^{-3} s^{-1}].

Poynting flux derived at the satellite altitude provides a measure of the net energy flow between the magnetosphere and the thermosphere/ionosphere below the satellite orbit. Recently, *Kelley et al.* [1991] have used the measurements from the HILAT satellite to determine the Poynting flux in the high-latitude thermosphere. They compared the field-aligned Poynting flux with the height-integrated Joule heating rate but made no allowance for neutral wind contributions. *Thayer and Vickrey* [1992] and *Deng et al.* [1993] have studied this concept further by including neutral wind feedback processes. By assuming some spatial homogeneity in the electrodynamics perpendicular to the magnetic field lines, it is found that the field-aligned Poynting flux derived at the spacecraft position is equal to the flux-tube-integrated energy conversion rate below the satellite orbit [*Thayer and Vickrey*, 1992; Gary et al., submitted manuscript, 1994]. This energy conversion rate can be determined by the Joule heating rate plus the work done on the neutrals by the Lorentz force (i.e., mechanical energy transfer

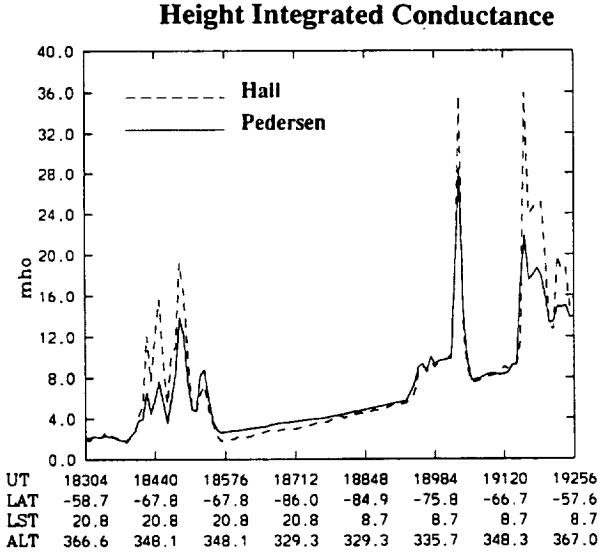

Figure 5. The height-integrated Hall conductivity (dashed line) and Pedersen conductivity (solid line) in (mho) along satellite orbit 1222.

rate). In this section, we study the relations between the Poynting flux, Joule heating rate and mechanical energy transfer rate.

The Poynting flux is defined by $S = E \times \delta B/\mu_o$, where E is the electric field measured at the satellite orbit and δB is perturbations of the geomagnetic field measured at the satellite track. The electric fields needed in determining the Poynting flux are derived from the ion velocities measured with the IDM and the RPA. The perturbation magnetic field is obtained as the difference between the magnetic field measured at the DE 2 satellite from MAG-B and a model of the Earth's intrinsic field derived from the Magsat mapping mission of the previous year. The accuracy of this perturbation magnetic field is limited by determining the base line of the Earth's intrinsic field. A several hundred nanotesla deviation of the perturbation field may occur due to the uncertainty in the attitude of the DE 2 spacecraft and the astromast upon which the magnetometer sensor is mounted. To compensate for these errors, a cubic spline was used to determine a new base line. The details of this technique are described by Gary et al. (submitted manuscript, 1994). This fitted curve is assumed to be a realistic base line for the intrinsic magnetic field.

Figure 6 shows the 1 second resolution data for the derived field-aligned Poynting flux along orbit 1222 with a nominal accuracy of 1.0 ergs/cm^{2}s. The flux is entirely downward (positive) throughout the pass, with the maximum value of 19.5 ergs/cm^{2}s occurring in the morning auroral oval near 67°S. In the evening auroral zone the flux is relatively small and irregular with an amplitude of about 5 ergs/cm^{2}s. The downward flux indicates that the electromagnetic energy associated with the Poynting flux is transferred from the magnetosphere to the thermosphere.

Figure 7 illustrates the model-calculated height-integrated energy conversion rate below the satellite orbit. This conversion rate is determined by integrating the local energy transfer rate defined as $J \cdot E$ over altitude below the satellite orbit, where the electrical current J is calculated by

$$J = \sigma \cdot (E + U \times B)$$

The electrical field E is derived from the ion drifts and magnetic field measurements along the satellite orbit. We have assumed that this electric field can map down to the lower thermosphere along the magnetic field lines. The neutral wind U is calculated from the VSH model. A comparison of this neutral wind with the DE 2 measurements at the satellite altitude is shown in Figure 2. The model-calculated energy conversion rate is in good agreement with the measured field-aligned Poynting flux. However, some differences exist in the polar cap where the model under-estimates the Poynting flux.

The reason for this difference may lie in the underestimation

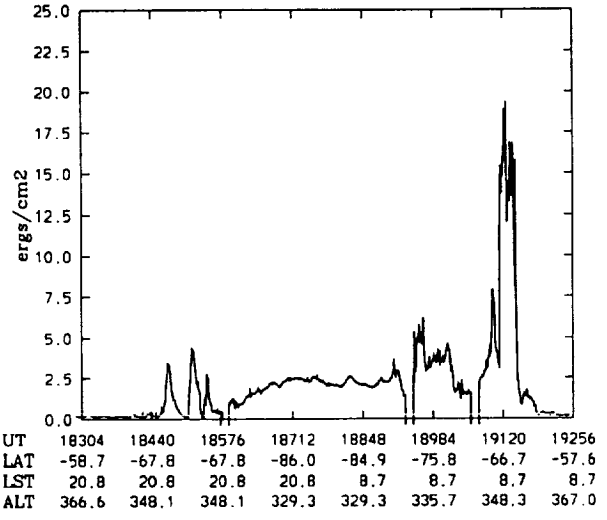

Figure 6. The field-aligned Poynting flux along satellite orbit 1222, this flux is derived from the DE 2 measurements.

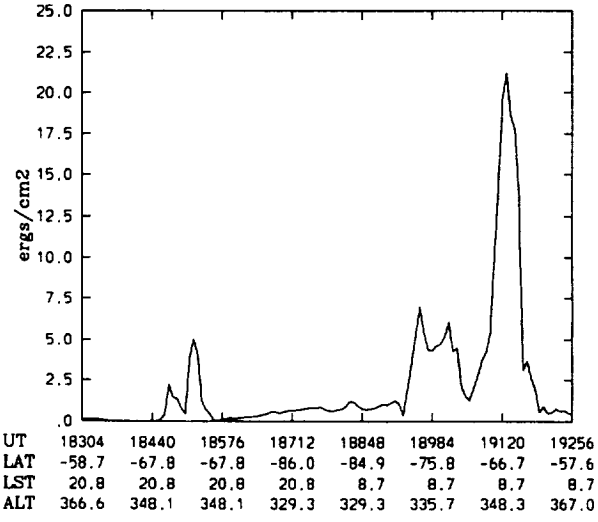

Figure 7. The model calculated height-integrated energy conversion rate for satellite orbit 1222.

of electron density in the polar cap due to the lack of transport effects in our one dimensional model. The antisunward ion drifts in the polar cap would move the daytime electron density into the nightside ionosphere, resulting in an increase in electron density in the satellite orbit plane which is located near the solar terminator. This transport effect is less pronounced in the auroral regions because the particle-enhanced electron density peaks at lower altitudes where transport is less important. Another contribution factor comes from the errors in determining the Poynting flux, which is relative larger for small values of the electric and perturbation magnetic fields, and at best is known to within about 15 percent. A discussion of the error involved in determining the Poynting flux from DE 2 is given by Gary et al. (submitted manuscript, 1994). Finally, the disagreement between VSH and DE 2 neutral wind in the polar cap (Figure 2) may also contribute to this difference. In general, the degree of agreement shown in this comparison gives us confidence in the extended satellite track code, allowing the model to be used to study the relative importance of the Joule heating rate and Lorentz energy transfer rate below the satellite track.

The height-integrated Joule heating rate is shown in Figure 8. The Joule heating rate is similar in magnitude to the energy conversion rate in the auroral regions, indicating that most of the electromagnetic energy imposed from the magnetosphere in these regions is dissipated by Joule heating in the lower thermosphere, and that only a small part of this energy is converted into the neutral mechanical energy through Lorentz energy transfer. Figure 9 shows the ratio of the calculated height-integrated Lorentz energy transfer rate to the height-integrated Joule heating rate. As expected, The contribution of this energy transfer rate is very small in the auroral regions (about 10%). However, it contributes significantly to the total energy conversion rate in the polar cap and can reach about 40% of the Joule heating rate across most of the polar cap. In this region, the neutral wind can act either as a generator, in which case the neutral wind releases energy and the Lorentz energy transfer

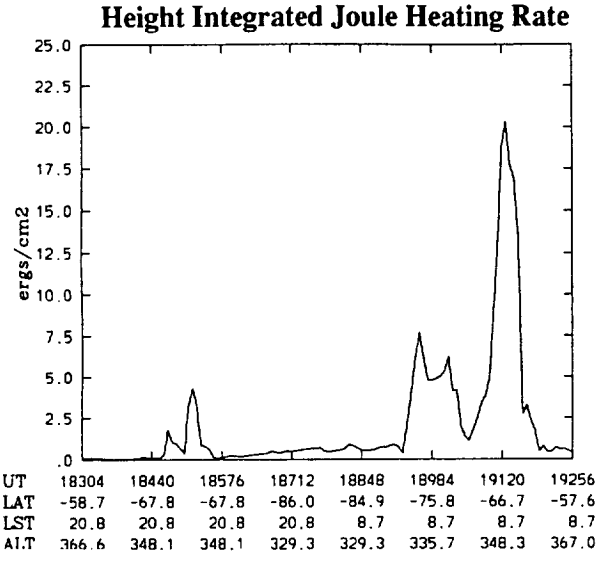

Figure 8. The same as Figure 7 except for height-integrated Joule heating rate.

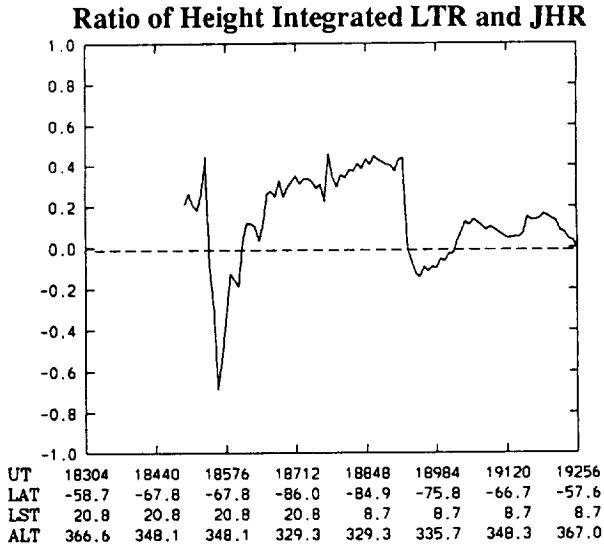

Figure 9. The ratio of height-integrated mechanical energy transfer rate (Lorentz transfer rate, LTR) to the height-integrated Joule heating rate (JHR) for satellite orbit 1222.

rate is negative, or as a load in which case the neutral wind gains energy and the Lorentz energy transfer rate is positive.

It should point out that these results are based on the neutral wind calculated from VSH model. The TIGCM upon which the VSH model has been based has yet to be validated in the lower thermosphere due to the lack of experimental data in this region. Therefore the neutral wind calculated from VSH model may not represent the real situation in the lower thermosphere. A further study is required with the use of comprehensive data set such as measurements that will be obtained from proposed TIMED mission.

6. An Overflight of Chatanika Site

In the previous section, we compared our model predictions with the satellite-measured Poynting flux. Another way to test these model predictions is to compare them with ground based observations. An overflight of the incoherent scatter radar facilities at Chatanika (65.1°N, 147.5°W) has provided such an opportunity to carry out a detailed comparison between the model calculations and radar measurements. The geometry of the satellite pass over Chatanika, Alaska is illustrated in Figure 10. For this close conjunction, the satellite was at an altitude of 740 km (orbit 1586), moving along the 146°W meridian at 1635 UT on November 18, 1981. The overflight occurred during southward IMF conditions, with a Kp of 3^+.

The electron flux spectra measured by the LAPI instrument on the DE 2 satellite at 1634:56 UT is displayed in Figure 11. This measurement was taken in the auroral regions where particle precipitation is strong. At this time the satellite was at about the geographic latitude of Chatanika but was about 2° off in longitude. The data were averaged over 8 seconds, which covers about 64 km. The variability of the spectra shape at different pitch angles is relatively small, thus implying an isotropic distribution. The maximum electron flux is about 10^7 (1/cm^2-s-ev-str) at lower energy. At higher energy, there are some

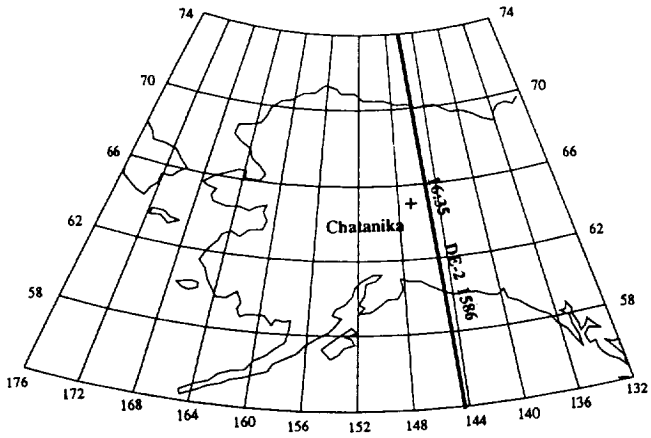

Figure 10. satellite track at 740 km altitude during the overflight of Chatanika, Alaska, on November 18, 1981.

small increases in hard auroral electron precipitation near 0.5 and 1 keV. Overall, the flux observed in this orbit is softer and less intense than that typically observed in auroral arcs. An average of this spectra over six pitch angles is used as an input to our model for determining the ionospheric structure below the satellite. For this calculation, we assumed that the observed electron flux was present for a sufficiently long time for a steady state electron density profile to be reached. The other inputs include the electron density and temperature measured by DE 2. Unfortunately, the neutral temperature measurement is not available for this period. We have used the satellite-measured O density as a guide to adjust the exospheric temperature in the MSIS-90 model so that it can reproduce the O density at the satellite orbit. Another uncertainty is the ion drifts which are also not available for this orbit. They are replaced by the radar measurements.

The incoherent scatter radar at Chatanika, Alaska, was making measurements during this overflight. The basic physical parameters measured by the radar are the electron density, electron and ion temperatures, and the plasma velocity along the line of sight of the radar beam. Data were obtained from 60 to about 800 km during this experiment. A detailed description of the equipment and the measurement capabilities of the radar is given by *Leadabrand et al.* [1972].

The overflight occurred on November 18, 1981. In this experiment, the radar was operated in the MITHRAS 2 model which provides a local measurement with a better time resolution [de la Beaujadiere et al., 1985, 1984]. This operation mode consists of a set of three positions, one parallel to magnetic filed and the others on either side of magnetic meridian at 70° elevation. The ion drift velocity is obtained by combining the line of sight velocities measured from these three positions. A long pulse was used for the velocity and temperature measurements and data were obtained at eight altitudes, starting at about 103 km and spaced 50 km apart. For the electron density measurements, a separate short (60 μs) pulse was used, which gives an altitude resolution of about 9 km. The conductivities and Joule heating are derived by using a neutral atmosphere model and neglecting the neutral winds. The electron density was corrected for temperature effects, and calibration was carried out at two levels (J. D. Kelly, private communication, 1994). The absolute calibration was performed using the Sheep Creek (near Fairbanks, Alaska) ionosonde F_0f_2 data. These data were compared to electron density measurements made with the Chatanika incoherent scatter radar on the average of once per year. This indicated agreement within 10%. The second calibration was a relative calibration performed by inserting a known level of noise at the end of every interpulse period. This calibration verified that there were no short term variations that were unaccounted for. Changes in receiver gain and background noise were eliminated in data processing using the inserted calibration noise pulse. More information about this period of data is provided by *Senior et al.* [1987] and *de la Beaujadiere et al.* [1985].

Figure 12 shows a comparison of our satellite track model-calculated electron density profile with the radar measurement during the overflight (1635 UT). The solid line indicates the electron density obtained from an average of the radar measurements between 1629 and 1642 UT. The error bars are obtained from the standard deviation from the average during this period. The dashed line is calculated from the satellite track model using the DE 2 measurements at 1635 UT, about 2° in longitude to the east of Chatanika. The satellite track model overestimates the electron density in the F region, while it underestimates the electron density in the E region. At high altitudes, the data agree well with the model predictions, indicating that the boundary condition determined by the satellite is close to the radar measurement. This overflight happened in the early morning (solar local time 0706), so the solar zenith angle at E region altitudes was large. Therefore the observed enhancement of E region electron density is mainly caused by energetic particle precipitation. Our model reproduces this increase quite well although it underestimates the magnitude.

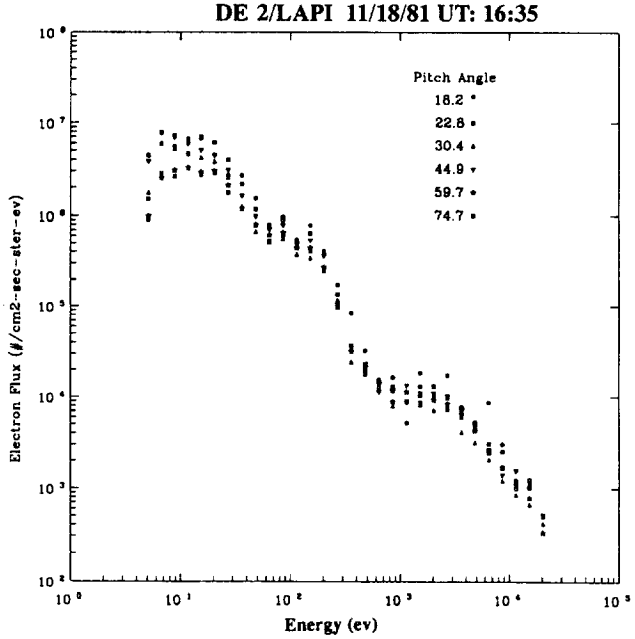

Figure 11. Eight-second average of electron spectra measured by the LAPI instrument around 1634:56 UT on November 18, 1981.

This underestimation may be caused by the use of a neutral atmosphere model, which has limited accuracy in the auroral regions during active geomagnetic conditions. It may also be explained by the changes of minor neutral constituents such as NO. In our model, we have only used the global mean value of the NO density. However, the NO density will increase significantly from its mean level in the auroral region due to the increases in the N_2 dissociation rate resulting from intense particle precipitation [*Roble*, 1992].

In the F-region, the model electron density is substantially higher (about 50%) than that of the radar measurements. Several factors contribute to this disagreement. First, as the altitude increases, horizontal transport effects become important. Since this overflight occurred on the equatorial side of the morning auroral oval, the convection is more likely to be in the sunward direction. The transport effect therefore would tend to move the lower electron density in the dark ionosphere into the morning auroral region, resulting in a decrease in electron density in this region. A one-dimensional model cannot include this effect and should therefore lead to an overestimation of the electron density. Another contributing factor is time dependent effects of the auroral event. As discussed by *Rees et al.* [1980], an auroral event is a time dependent process in which various ion species respond to particle bombardment at different rates. To model this process rigorously requires a knowledge of the time history of the precipitation electron flux. It is possible that a steady state is not reached at the time of the overflight due to the sluggish response of the *F* region ionization. As a result, the electron density remains lower than that in the steady state, where it has higher value due to the decrease in the electron

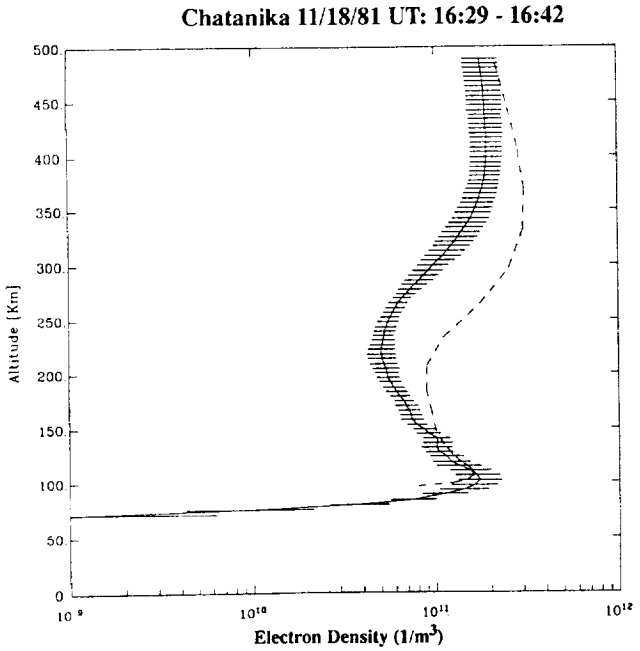

Figure 12. Comparison of radar measured electron density profile (solid line) with the model calculations (dashed line) during the overflight at 1635 UT. The electron density profile is obtained from an average of the radar measurements between 1629 and 1642 UT. The error bars are obtained from the standard deviation of the average during this period.

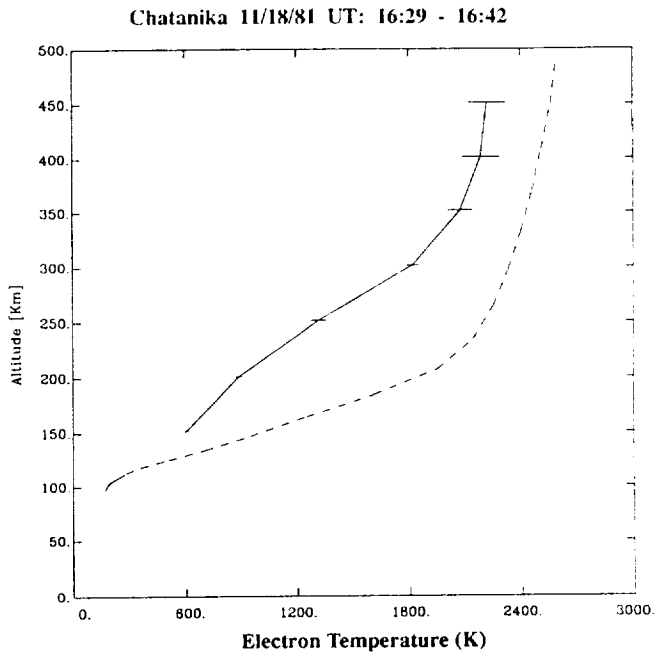

Figure 13. The same as Figure 12 except for the electron temperature.

temperature. Finally, the 2° longitudinal offset of the satellite pass over the Chatanika site may also contribute to this disagreement. Overall, despite the discrepancy between the experimental result and our model calculation, there is a good general agreement as to the morphology of the electron density profile.

The comparison of electron temperatures is shown in Figure 13. While crude agreement in shape is seen, a significant difference between the radar-measured temperatures (solid line) and the modeled temperatures (dashed line) of ~400 K exists

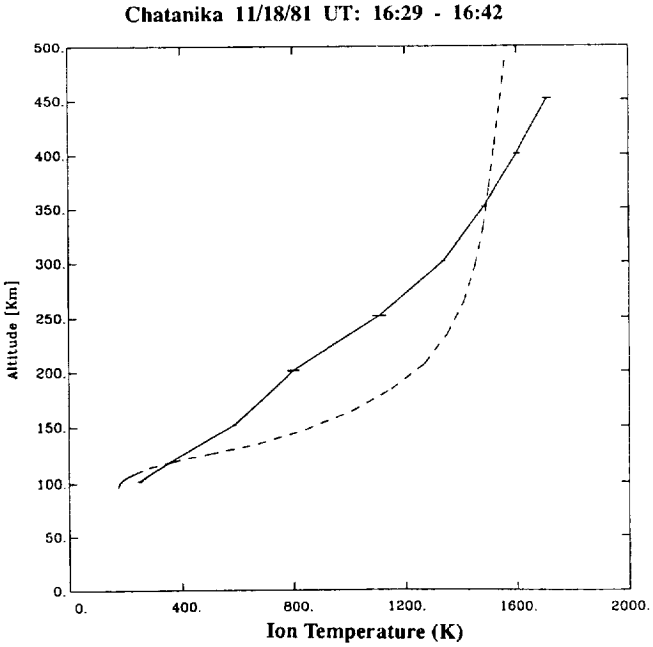

Figure 14. The same as Figure 12 except for the ion temperature.

at the upper altitudes, with the modeled temperatures being higher than the radar measurements. Since the satellite measurement is used as the upper boundary condition for the satellite track code, this discrepancy may account for some of the disagreement at lower altitudes. It is impossible to determine whether instrumental effects or spatial changes in the electron temperature distribution are responsible for the discrepancy. The ion temperatures are illustrated in Figure 14. The model overestimates the ion temperature in the region below 300 km by as much as 400 K. Since the ion temperature is closely coupled with the neutral temperature in this region, most of difference is due to the overestimation of neutral temperature in the *F* region below the satellite orbit.

The comparison of radar-measured and modeled Hall and Pedersen conductivities are depicted in Figures 15 and 16, respectively. There is a good agreement between the model calculations and the radar measurements. Finally, we present a comparison between radar-derived Joule heating rates and the model calculation in Figure 17. In the model calculation, the neutral wind has been neglected. This is in agreement with the assumption used to obtain Joule heating rate from the radar data. As expected, good agreement is attained in the lower thermosphere, which provides confidence for the results obtained in the previous section. The difference at the higher altitudes is mainly caused by the overestimation of the electron density. Since the Joule heating peaks in the lower thermosphere and decreases rapidly with increasing altitude, this disagreement does not have a significant effect on the height-integrated Joule heating rate (the value of height-integrated Joule heating rate are about 1.38 and 1.51 ergs/cm^2-s, calculated from radar measurements and model predictions respectively).

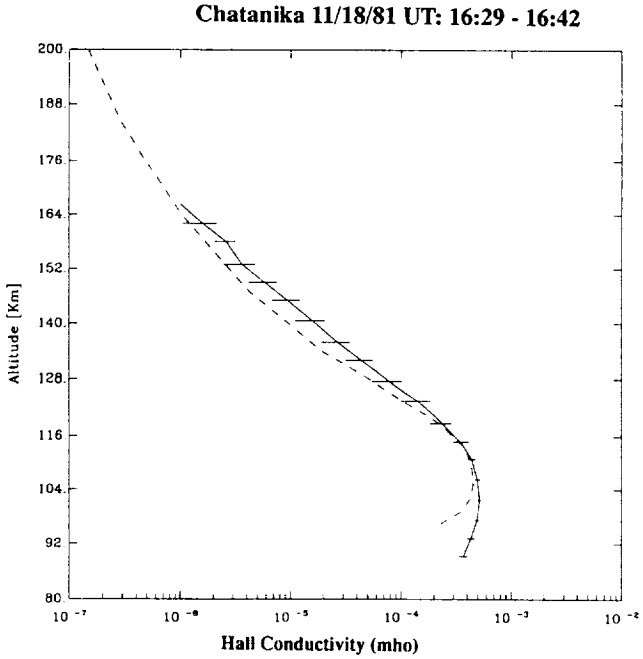

Figure 15. Comparison of derived Hall conductivity (solid line) from the radar measurement with the model calculation (dash line) at the overflight. The Hall conductivity profile is obtained from an average of derived Hall conductivity between 1629 and 1642 UT. The error bars are obtained from the standard deviation of the average during this period.

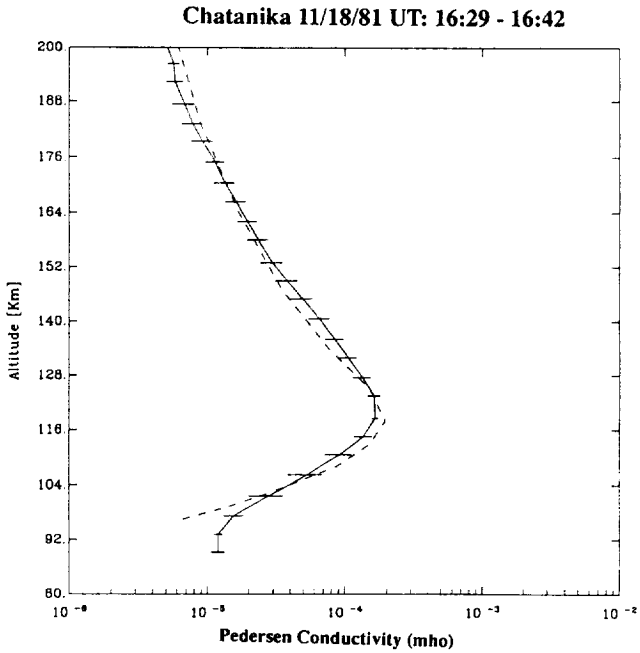

Figure 16. The same as Figure 15 except for the Pedersen conductivity.

7. Summary

We have developed a satellite track model. The major model inputs are measurements of the electron precipitation flux to determine ionization rates and of ion drifts to determine the Joule heating rates. The model has been used to study the ionospheric structure below the satellite pass (orbit 1222) and

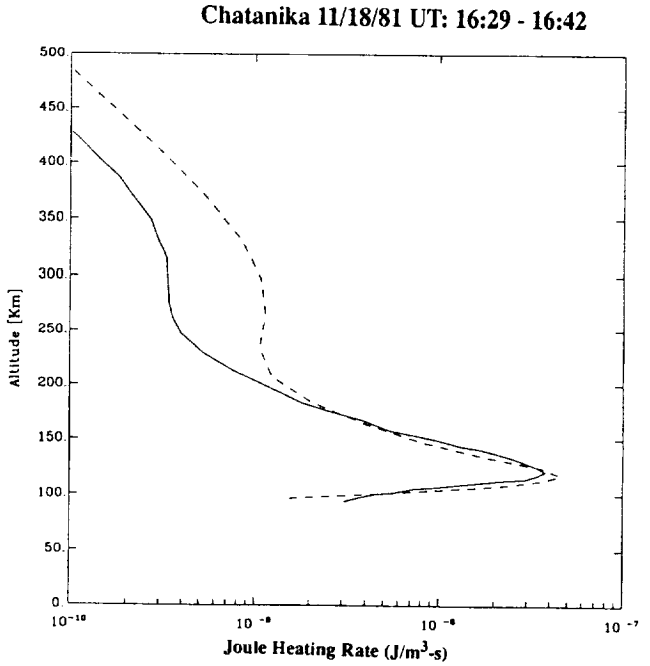

Figure 17. The same as Figure 15 except for the Joule Heating Rate.

has been compared with the incoherent scatter radar measurements at Chatanika, Alaska during a DE 2 overflight. Our principal results may be listed as follows:

1. The model has demonstrated an ability to map the DE 2 satellite measurements into the lower thermosphere-ionosphere.

2. A good first-order agreement has been reached between the DE 2 derived field-aligned Poynting flux and the height-integrated energy conversion rate, yielding confidence in the calculated lower thermospheric conductivities and Joule heating rates.

3. The study of electromagnetic energy budget below the satellite orbit indicates that most of the electric energy from the magnetosphere is dissipated by Joule heating in the auroral region. Only a small part is converted into the neutral wind mechanical energy in this region. However, the neutral wind contributes significantly to the electromagnetic energy budget in the polar cap.

4. Comparison between the radar measurements and model predictions indicates a good agreement in lower thermospheric conductivities and Joule heating rates.

Acknowledgments. This study was supported by NASA grant NAGW-3457 and NAG5-465, by NSF grant ATM-8918476 and ATM-9096134, and USAF grant F19628-89-K-0026 to the University of Michigan. The study also made use of the CEDAR database at NCAR, which, along with Chatanika radar, is supported by the National Science Foundation. The authors are grateful to O. de la Beaujardiere and J. D. Kelly for useful discussions about the Chatanika data. We gratefully acknowledge W. B. Hanson, R. A. Heelis, and J. A. Slavin for providing their DE 2 data. We also would like to thank Dr. R. A. Heelis for useful discussions and suggestions.

The Editor thanks C. G. Fesen and M. J. Buonsanto for their assistance in evaluating this paper.

References

Carignan, G. R., B. P. Block, J. C. Maurer, A. E. Hedin, C. A. Reber, and N. W. Spencer, The Neutral Mass Spectrometer on Dynamics Explorer, *Space Instrum.*, *5*, 429-442, 1981.

de la Beaujardiere, O., V. B. Wickwar, M.J. Baron, J. Holt, R.M. Wand, W.L. Oliver, P. Bauer, M. Blanc, C. Senior, D. Alcayde, G. Caudal, J. Foster, E. Nielsen, and R. Heelis, MITHRAS: A brief description, *Radio Science*, *19*, 665-673, 1984.

de la Beaujardiere, O., V. B. Wickwar, G. Caudal, J. M. Holt, J. D. Craven, L.A. Frank, L.H. Brace, D. S. Evans, J. D. Winningham, and R. A. Heels, Universal time dependence of nighttime F region densities at high latitudes, *J. Geophys. Res.*, *90*, 4319-4332, 1985.

Deng, W., T.L. Killeen, A.G. Burns, R.G. Roble, J, Slavin, and L.E. Wharton, The effects of neutral inertia on ionospheric currents in the high latitude thermosphere following a geomagnetic storm, J. *Geophys. Res. 98*, 7775-7790, 1993.

Emery, B. A., R. G. Roble, E. C. Ridley, T. L. Killeen, M. H. Rees., J. D. Winningham, G. R. Carignan, P. B. Hays, R. A. Heelis, W. B. Hanson, N. W. Spencer, L. H. Brace and M. Sugiura, Thermospheric and Ionospheric Structure of the Southern Hemisphere Polar Cap on October 21, 1981, as Determined From Dynamics Explorer 2 Satellite Data, *J. Geophys. Res.*, *90*, 6553-6566, 1985.

Farthing, W. H., M. Sugiura, B. G. Ledley, and L. J. Cahill, Jr., Magnetic field observations on DE-A and -B, *Space Instrum.*, *5*, 551-560, 1981.

Foster, J., An empirical electric field model derived from Chatanika radar data, *J. Geophys. Res.*, *88*, 981-987, 1983.

Foster, J. C., J.-P. St.-Maurice and V. J. Abreu, Joule heating at high latitudes, *J. Geophys. Res.*, 88, 4885-4896, 1983.

Fuller-Rowell, T. J., and D. S. Evans, Height integrated Pedersen and Hall conductivity patterns inferred from the TIROS-NOAA satellite data, *J. Geophys. Res 92.*, 7606-7618, 1987.

Hanson, W. B., R. A. Heelis, R. A. Power, C. R. Lippincott, D. R. Zachary, B. J. Holt, L. H. Harmon, and S. Sanatani, The Retarding Potential Analyzer for Dynamics Explorer-B, *Space Sci. Instrum.*, *5*, 503-510, 1981.

Hays, P. B., T. L. Killeen, and B. C. Kennedy, The Fabry-Perot Interferometer on Dynamics Explorer, *Space Instrum.*, *5*, 395-416, 1981.

Hays, P. B., T. L. Killeen, N. W. Spencer, L. E. Wharton, R. G. Roble, B. E. Emery, T. J. Fuller-Rowell, D. Rees, L. A. Frank, and J. D. Craven, Observations of the dynamics of the polar thermosphere, J. *Geophys. Res.*, *89*, 5597-5612, 1984.

Hedin, A.E., M.A. Biondi, R.G. Burnside, G. Hernandez, R.M. Johnson, T.L. Killeen, C. Mazaudier, J.W. Meriwether, J.E. Salah, R.J. Sica, R.W. Smith, N.W. Spencer, V.B. Wickwar, and T.S. Virdi, Revised global model of thermosphere winds using satellite and ground-based observations, *J. Geophys. Res.*, *96*, 7657-7688, 1991.

Heelis, R. A., W. B. Hanson, C. R. Lippincott, D. R. Zuccaro, L. H. Harmon, B. J. Holt, J. E. Doherty, and R. A. Power, The Ion Drift Meter for Dynamics Explorer-B, *Space Instrum.*, *5* 511-522, 1981.

Heelis, R. A., J. K. Lowell, and R. W. Spiro, A model of the high-latitude ionospheric convection pattern, J. Geophys. Res., 87, 6339-6345, 1982.

Heelis, R. A. and W. R. Coley, Global and local Joule heating effects seen by DE 2, *J. Geophys. Res.*, *93*, 7551-7557, 1988.

Heppner, J. P., Empirical models of high-latitude electric fields, *J. Geophys. Res.*, *82*, 1115-1125, 1977.

Hinteregger, H. E., Representations of solar EUV fluxes for aeronomical applications, *Adv. Space Res.*, *86*, 801-813, 1981.

Kelley, M. C., D. J. Knudsen and J. F. Vickery, Poynting flux measurements on a satellite: A diagnostic tool for space research, *J. Geophys. Res.*, *96*, 201-207, 1991.

Killeen, T. L., R. W. Smith, N. W. Spencer, J. W. Meriwether, D. Rees, G. Hernandez, P. B. Hays, L. L. Cogger, D. P. Sipler, M. A. Biondi and C. A. Tepley, Mean neutral circulation in the winter polar F region, *J. Geophys. Res.*, *91*, 1633-1649, 1986.

Killeen, T. L., R. G. Roble, and N. W. Spencer, A computer model of global thermospheric winds and temperatures, *Adv. Space Res 7.*, 207-215, 1987

Killeen, T. L. and R. G. Roble, Thermosphere Dynamics driven by magnetospheric sources: contributions from the first five years of the Dynamics Explorer program, *Rev. Geophys. Space Phys.*, 329-367, 1988.

Krehbiel, J. P., L. H. Brace, R. F. Theis, W. H. Pinkus, and R. B. Kaplan, Dynamics Explorer Langmuir Probe Instrument, *Space Instrum.*, *5*, 493-502, 1981.

Leadabrand, M. J. Baron, J. Petriceks and H. F. Bates, Chatanika, Alaska, auroral-zone incoherent-scatter facility, *Radio Science 7*, 747-756, 1972.

Rees, M.H., Auroral ionization and excitation by incident energetic electrons, *Planet. Space Sci.*, *11*, 1209-1218, 1963.

Rees, M.H., Auroral electrons, *Space Sci. Rev., 10*, 413-441, 1969.

Rees, M. H., R. G. Roble, J. Kopp, V. J. Abreu, L. H. Brace, H. C. Brandon, R. A. Heelis, R. A. Hoffman, D. C. Kayser, and D. W. Rusch, The spatial-temporal ambiguity in auroral modeling, *J. Geophys. Res., 85*, 1235-1245, 1980.

Rees, M. H., B. A. Emery, R. G. Roble, and K. Stamnes, Neutral and ion gas heating by auroral electron precipitation, *J. Geophys. Res., 88*, 6289-6300, 1983.

Richards, P. G., and D. G. Torr, Ratios of photoelectron to EUV ionization rates for aeronomic studies. *J. Geophys. Res., 93*, 4060, 1988.

Richmond, A. D. and Y. Kamide, Mapping electrodynamic features of high-latitude ionosphere from localized observations: Technique, *J. Geophys. Res., 93*, 5741-5759, 1988.

Roble, R. G., B. A. Emery, R. E. Dickinson, E. C. Ridley, T. L. Killeen, P. B. Hays, G. R. Carignan, and N. W. Spencer, Thermospheric circulation, temperature and compositional structure of the southern hemisphere polar cap during October-November, 1981, *J. Geophys. Res., 89*, 9057-9068, 1984.

Roble, R. G., B.A. Emery, T.L. Killeen, G.C. Reid, S. Solomon, R.R. Garcia, D.S. Evans, P.B. Hays, G.R. Carignan, R.A. Heelis, W.B. Hanson, D.J. Winningham, N.W. Spencer, and L.H. Brace, Joule heating in the mesosphere and thermosphere during the July, 13, 1982, solar proton event, *J. Geophys. Res., 92*, 6083-6090, 1987a.

Roble, R. G., E. C. Ridley and R. E. Dickinson, On the global mean structure of the thermosphere, J. Geophys. Res., 92, 8745-8758, 1987b.

Roble, R. G., and E. C. Ridley, An auroral model of the NCAR thermospheric general circulation model (TGCM), *Annales Geophysicae, 5A, (6)*, 369-382, 1987c.

Roble, R. G., and R. E. Dickinson, How will changes in carbon dioxide and methane modify the mean structure of the mesosphere and thermosphere?, *Geophys. Res. Lett., 16*, 1441-1444, 1989

Roble, R. G., The polar lower thermosphere, *Planet. Space Sci. 40*, 271-297, 1992.

Schunk, R. W. and A. F. Nagy, Electron temperature in the F region of the ionosphere: Theory and observation, Rev. Geophys., 16, 355, 1978.

Senior, C., J. R. Sharber, O, de la Beaujardiere, R. A. Heelis, D. S. Evans, J. D. Winningham, M. Sugiura, and W. R. Hoegy, E and F region study of the evening sector auroral oval: A Chatanika/ Dynamics Explorer 2/ NOAA 6 comparison, *J. Geophys. Res., 92*, 2477-2494, 1987.

Spencer, N. W., L. E. Wharton, H. B. Niemann, A. E. Hedin, G. R. Carignan, and J. C. Maurer, The Dynamics Explorer Wind and Temperature Spectrometer, *Space Instrum., 5*, 417-428, 1981.

Thayer, J. P. and J. F. Vickrey, On the contribution of thermospheric neutral wind to high latitude energetics, *Geophys. Res. Lett., 19*, 265-268, 1992.

Torr, M. R., and D. G. Torr, Ionization frequencies for solar cycle 21: revised, *J. Geophys. Res., 90*, 6675-6678, 1985.

Torr, M. R., D. G. Torr., R. A. Ong, and Hintetegger, Ionization frequencies for major thermospheric constituents as a function of solar cycle 21, *Geophys. Res. Lett., 6*, 771-774, 1979.

Torr, M. R., D. G. Torr, and Hinteregger, Solar flux variability in the Schumann-Runge continuum as function of solar cycle 21, *J. Geophys. Res., 85*, 1633-1649, 1980.

Wallis, D. D. and E. E. Budzinski, Empirical models of height-integrated conductivity, *J. Geophys. Res., 86*, 125-137, 1981.

Winningham, J. D., J. L. Burch, N. Eaker, V. A. Blevins, and R. A. Hoffman, The Low Altitude Plasma Instrument (LAPI), *Space Instrum.*, 5, 465-476, 1981.

A. G. Burns, R. M. Johnson, and T. L. Killeen, Space Physics Research Laboratory, Department of Atmospheric, Oceanic and Space Sciences, University of Michigan, Ann Arbor, MI 48109-2143.

W. Deng, Atmospheric Sciences Group, Haystack Observatory, Massachusetts Institute of Technology, Westford, MA 01886. (e-mail: Internet: wdg@hyperion.haystack.edu)

B. A. Emery and R. G. Roble, National Center for Atmospheric Research Boulder, CO 80307.

J. B. Gary, University of Texas at Dallas, Richardson, TX 75803.

J. D. Winningham, Department of Space Sciences, Southwest Research Institute, San Antonio, TX 78284.

(Received October 11, 1993; revised August 4, 1994; accepted August 10, 1994.)